Short-range order and chemical compositions of glasses along the basaltic-rhyolite sub-alkaline join by Raman and FTIR spectroscopies

Francesco Radica [a,b,*], Michele Cassetta [c,d,**], Gianluca Iezzi [a,b,e], Alessandro Pisello [f], Francesco Vetere [g], Alessandro Del Vecchio [a], Mariangela Cestelli Guidi [h], Brent T. Poe [a,e]

[a] *Dipartimento INGEO (Ingegneria & Geologia), Università di Chieti-Pescara 'G. d'Annunzio', Chieti, Italy*
[b] *UdA-TechLab, Research Center, University "G. d'Annunzio" of Chieti-Pescara, 66100 Chieti, Italy*
[c] *Department of Industrial Engineering, University of Trento, I-38122 Trento, Italy*
[d] *Department of Engineering for Innovation Medicine, University of Verona, I-37134 Verona, Italy*
[e] *Istituto Nazionale di Geofisica e Vulcanologia INGV, Rome, Italy*
[f] *Department of Physics and Geology, University of Perugia, Piazza Università 1, 06100 Perugia, Italy*
[g] *Department of Physical Sciences, Earth and Environment, University of Siena, 53100, Italy*
[h] *INFN - Istituto Nazionale di Fisica Nucleare, Frascati, Italy*

ARTICLE INFO

ABSTRACT

Six sub-alkaline glasses with compositions progressively shifting from the tholeiitic basalt (B_{100}) end-member to the rhyolite (R_{100}) end-member were investigated and analysed in the same frequency domain by both Raman and FTIR. This approach highlights spectroscopic similarities and differences such as positions, widths and intensities of Raman and FTIR bands, which may also exhibit significant overlapping. Both the Raman and FTIR spectra show several peaks grouped in three main vibrational windows: 200–650 (low frequency region, named F-I in this study), 650–850 (intermediate region, F-II) and 850–1250 cm^{-1} (high-frequency region, F-III). In line with previous investigations, the F-I interval can be ascribed to vibrational modes involving rings of tetrahedrally coordinated cations linked by bridging oxygens. It can be fitted with three components, whereas F-II involves the motion of Si atoms within its oxygen cage and is adequately represented by two components. Finally, F-III contains different T-O (T = tetrahedrally coordinated network-forming cation) stretching bands that can be tied to the overall degree of polymerization of the glass and are fitted with four components. In some glasses, the three and the two components within F-I and F-II are identifiable in both Raman and FTIR spectra; in cases of strong peak overlap, these peaks can be complementary to one another towards our interpretation of the molecular arrangement(s) in these glasses. Indeed, the positions of the four components in F-III are first constrained in the Raman spectra, which are more identifiable, then further refined using available Raman spectra for corresponding chemically simple silicate systems. The nine fitted components can reproduce the Raman and FTIR spectra extremely well.

As a function of the amount of SiO_2, the positions and intensities of the three low frequency components progressively shift in both Raman and FTIR. Similarly, the two bands in the F-II intermediate region exhibit a monotonic shifting of their positions. Indeed, the components at high frequency display less significant shifting of their positions as a function of SiO_2, while their intensities change more markedly in the Raman spectrum compared to those for FTIR. The vibrational components measured in this study provide a referenced dataset of assignations of the most abundant natural volcanic glasses. Therefore, it provides a diagnostic tool based on the cross-validation of Raman and FTIR spectra to quickly identify the glass chemistry, offering the possibility to expand the applicability of remote investigations.

1. Introduction

Glassy silicate phases are among the main constituents in volcanic rocks participating in a large portion of the Earth's crust (Middlemost, 1972; Lemaitre et al., 2002) and planetary bodies (Minitti and Hamilton, 2010). They mainly originate from the relatively rapid cooling of silicate melts. Thus, glass structure can be considered a proxy for liquid structure frozen along a temperature-time path avoiding any crystalline phase formation (*e.g.* Dingwell and Webb, 1989; Cassetta et al., 2021). Typically, they are characterized by a lack in the long-range order (LRO) and exhibit only a limited ordered distribution on a specific length scale of about 10 Å, defined as short-range order (SRO) (Mysen and Richet, 2005; Calas et al., 2006; Neuville et al., 2022). The atomic distribution in any crystalline structure can be very accurately measured by using different techniques such as: X-ray diffraction methods, nuclear magnetic resonance (NMR), as well as neutron and electron diffractions (Maekawa et al., 1991; Miletich and Malcherek, 2005; Cole and Ross, 2021).

However, vibrational spectroscopic techniques such as Raman and FTIR are better suited for examining SRO. They are particularly effective in characterizing the structure of glasses as they have been used first on relatively simple (1–3 oxide components) crystalline phases in order to identify the vibrational features of stoichiometric-equivalent non-crystalline compounds (Beran and Libowitzky, 2004; Neuville et al., 2022). In addition, in the last few decades *ab initio* methods such as Density Functional Theory have been increasingly more reliable at reproducing the vibrational spectra of materials with ever increasing chemical and structural complexity (Le Losq et al., 2021; Neuville et al., 2022). Alternatively, many experimental studies have focussed on untangling the complex vibrational spectra of multicomponent glasses using simplified chemical systems, with well-defined atomic substitutions along compositional joins (Dufresne et al., 2009; Meneses et al., 2013; Mocioiu et al., 2013). These investigations have strongly improved our knowledge of the SRO of natural and technical glasses. Still, a general picture of chemically complex natural glasses containing all of the common and most abundant oxides (SiO_2, TiO_2, Al_2O_3, Fe_2O_3, MgO, FeO, CaO, Na_2O and K_2O) is scarce and remains puzzling (for Raman spectroscopy: Di Genova et al., 2015; González-García et al., 2020; Cassetta et al., 2024; for infrared spectroscopy: King et al., 2004; Morlok et al., 2017; Pisello et al., 2019, 2022).

Six sub-alkaline volcanic glasses are investigated using Raman and FTIR transmission spectroscopy between 180 and 1300 cm-1 to shed new light on the SRO of the most abundant naturally occurring naturally occurring glasses on Earth and analogue planetary systems. The oxide abundances (wt%) of these glasses progressively and linearly shift from the tholeiitic basalt (B_{100}) end-member towards the rhyolite (R_{100}) end-member. The most easily identifiable bands in both Raman and FTIR were modelled as symmetric Gaussian peaks. This allows us to quantify spectral features in terms of position, width and intensity (expressed as normalized area). The SRO similarities, differences and peculiarities observed here can be used to identify the atomic structure and chemical attributes of glassy phases in volcanic and shocked materials, either in a laboratory or remotely. These outcomes are pivotal for the study of extra-terrestrial bodies (Morlok et al., 2017; Rho et al., 2018; Pisello et al., 2022) or inaccessible terrestrial areas when investigated by IR remote-sensing methods.

2. Materials and methods

2.1. Analysed glasses

The six glasses analysed here are those synthesized and characterized by SEM, EPMA, Karl-Fisher and wet iron speciation (Wilson method) in Vetere et al. (2013, 2015). Briefly, the two B_{100} and R_{100} end-members were prepared by two cycles of melting (1600 °C), with intermediate quenching (from 1300 °C) and powdering; the third cycle of melting and

quenching produced several grams of the two fully glassy end-members. These two poles were then mixed to produce the four intermediate bulk compositions $B_{80}R_{20}$, $B_{60}R_{40}$, $B_{40}R_{60}$ and $B_{20}R_{80}$, which were used to prepare the corresponding glasses following the previous procedure. The major oxide components of the glasses (determined by EPMA-WDS) are reported in Table 1. The composition of these glasses aligns along the sub-alkaline trend in the TAS diagram (Table 1; Fig. 1). The largest pieces of each glass were cut into rectangular prisms with thicknesses close to 1 mm and lengths ranging from 4.5 to 6.23 mm (Table 1). These crystal-free glassy prisms were used here to record both Raman and FTIR spectra.

2.2. Acquisitions of Raman and FTIR spectra

The Raman spectra were acquired at the Centro Piattaforme Tecnologiche (University of Verona) with a confocal setup, with a back-scattering geometry and using a double subtractive single configuration for a triple-axis monochromator (Horiba-Jobin Yvon, model T-64000). The scattered light was filtered by three holographic gratings (1800 lines/mm) and detected by a CCD (1024 × 256 pixels) cooled by liquid nitrogen. The exciting radiation was provided by a mixed Ar-Kr ion gas laser (Spectra Physics Satellite 2018 RM) set at 514.5 nm. The laser beam was focused onto a spot of about 2 μm using a 50× objective with NA = 0.50. The power on the sample surface is ~10 mW. Measurements were done at room conditions. The FTIR transmission spectra were acquired at the DAFNE laboratory at Istituto Nazionale di Fisica Nucleare – Laboratori Nazionali di Frascati (Rome) using a Bruker Hyperion 3000 IR microscope 15× objective, DLaTGS wide range detector. The spectra were acquired averaging 128 scans with a nominal spectral resolution of 4 cm^{-1}.

2.3. Spectra pre-processing

Raw Raman and FTIR spectra are displayed in Fig. S1 and are available online in the data repository. In order to quantify the position, width and intensity of all components (see Results section), a few pre-processing steps were carried out on the whole range of each Raman and FTIR spectrum. A summary of these steps is displayed in Fig. S2 for

Table 1

Major oxide compositions, iron speciation, NBO/T, dimensions and density of the analysed glass prims.

Sample	B_{100}	$B_{80}R_{20}$	$B_{60}R_{40}$	$B_{40}R_{60}$	$B_{20}R_{80}$	R_{100}
SiO_2	48.02	53.01	57.97	62.73	67.91	73.97
TiO_2	0.98	0.8	0.65	0.46	0.29	0.12
Al_2O_3	15.59	14.99	14.62	14.05	13.59	13.48
Fe_2O_3	11.37	9.49	7.73	6.02	4.1	2.29
MnO	0.18	0.15	0.13	0.12	0.11	0.08
MgO	9.42	7.58	5.81	4.01	2.18	0.44
CaO	13.2	10.79	8.46	6.07	3.63	1.36
Na_2O	1.79	2.18	2.59	2.95	3.29	3.75
K_2O	0.04	1.02	1.99	3.02	3.99	4.89
P_2O_5	0.06	0.02	0.04	0.02	0.02	0.03
TOT	100.65	100.03	99.99	99.45	99.11	100.41
Fe^{2+}/Fe^{total}	0.386	0.449	0.434	0.412	0.424	0.343
NBO/T	0.53	0.46	0.36	0.25	0.15	0.04
prism weight (g)	0.062	0.058	0.063	0.055	0.077	0.084
prism length$_1$ (mm)	4.79	4.89	4.5	5.05	5.27	6.23
prism length$_2$ (mm)	4.8	3.37	4.08	3.36	4.66	6.24
prism thickness (mm)	0.96	1.32	1.31	1.32	1.32	0.97
prism density (g/cm^3)	2.804	2.648	2.599	2.46	2.366	2.238

Footnotes: chemical compositions of glasses by EPMA-WDS are from Vetere et al. (2013, 2015); Fe^{2+}/Fe^{tot} was determined for each sample using a modified Wilson method as described in Vetere et al. (2013); NBO/T determined assuming all Si, Ti, Al, Fe^{3+} are tetrahedrally coordinated network forming cations (see Mysen, 1983).
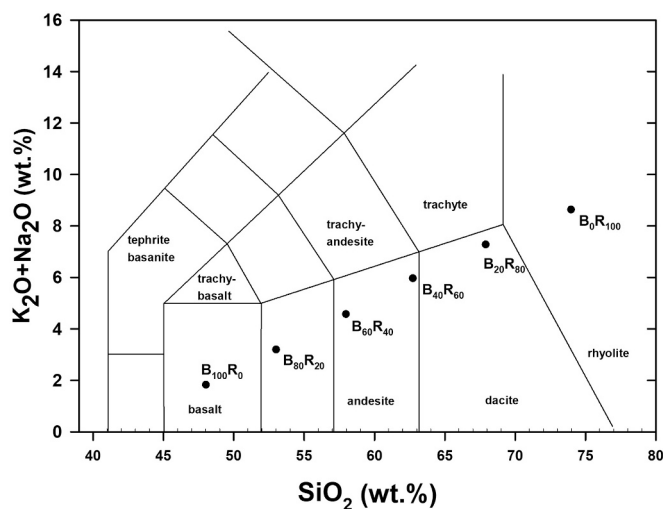
Fig. 1. Classification of the six glasses in the TAS diagram.

the glass $B_{40}R_{60}$. For the Raman spectra, we first applied the correction for temperature and excitation line using the Long approach (Long, 1977):

$$I(\omega) = I^{obs} \left\{ \omega_0^3 \, \omega \, \frac{[1 - exp(-hc\omega/k_BT)]}{(\omega_0 - \omega)^4} \right\} \qquad (1)$$

where h and k_B are the Plank and Boltzmann constants, respectively, c is the speed of light, T is the absolute temperature (in kelvin), ω_0 is the laser frequency (514.5 nm, thus $\omega_0 = 19{,}435.1 \text{ cm}^{-1}$), whilst ω the observed frequency in cm^{-1}. A slight smoothing was also applied to the Raman signal to reduce systematic noise.

Background modelling was one of the most challenging tasks when dealing with both Raman and especially FTIR transmission spectra. After several trials using different interpolation methods and anchor points, we opted for a modified version of the model first introduced by Mercier et al. (2009, 2010) and recently used by González-García et al. (2020). Background reduction was performed in the same way for both Raman and FTIR spectra by subtracting three simple linear baselines anchored to 4 points, in line with previous investigations (Giordano et al., 2020; González-García et al., 2020). The three baseline intervals correspond to three well defined regions labelled hereafter F-I, F-II and F-III; each region has very similar Raman and FTIR spectroscopic features (Fig. S2). The baseline endpoints were anchored to the spectra at 4 minima located around 200, 650, 850 and 1250 cm^{-1}, and then subtracted in the spectral range from 200 cm^{-1} to 1250 cm^{-1}. The baseline for the FTIR spectra in the 850–1250 cm^{-1} range could be more complex, but without a clear spectroscopic constraint, it was modelled with a simple straight line consistent with the same region for the Raman spectra. Finally, each spectrum was normalized to the maximum intensity after background subtraction (Fig. S2).

2.4. Fitting strategy to derive Raman and FTIR band components

The position, full-width at half-maximum (FWHM) and integrated intensity (area %) of these bands can be quantified only by fitting their components due to their moderate to high degree of overlapping (see Fig. 3). Consequently, the fitting strategy was adopted as follows: i) as few as possible Gaussian shaped components were used to reproduce the measured spectra, ii) spectroscopic components belonging to the same spectral subregion were constrained to share the same peak width, iii) the most evident components were identified starting from the glass that showed lesser band overlapping either by Raman or FTIR (*i.e.* the R_{100} in both cases) and iv) the remaining and severely overlapped components were identified by considering the position of the corresponding and

more straightforward identifiable band(s) on other glasses along the investigated join and/or retrieved from similar bands reported in the literature (see below).

3. Results

Fig. 2a and b report the stacked plot of the processed Raman and FTIR spectra. Fig. 2c and d report the corresponding intensity heat maps highlighting the global variations of relative intensities as a function of both composition and spectroscopic method. The Raman and FTIR spectra of the same glass are significantly similar; also, Raman and FTIR spectra follow similar spectroscopic variations induced by the compositional variation from B_{100} to R_{100} (Fig. 2c and d). The adopted processing method and background modelling (see above) identify three feature intervals between 200 cm^{-1} and 1250 cm^{-1} in each of the spectra: i) a moderately sharp one located between 200 and 650 cm^{-1} with medium to high intensities (F-I: feature I), ii) the least intense and narrowest between 650 and 850 cm^{-1} (F-II: feature II), and iii) a third broad and intense one between 850 and 1250 cm^{-1} (F-III: feature III).

The differences in intensities of the low- and high-frequency regions are more marked in Raman spectra than in FTIR spectra (Fig. 2). Specifically, as SiO_2 content increases (from B_{100} to R_{100}), the integrated intensity of the F-I region increases and that of the F-III region decreases more significantly among the Raman spectra compared to FTIR (Fig. 2). Additionally, in the Raman spectra the position of the maximum in the F-I region also shifts to lower frequency. The two F-II bands are more intense and appreciable in the FTIR spectra than in Raman; nonetheless, in both methods their positions show a blue-shift with increasing SiO_2 (Fig. 2). In both spectroscopic methods, the third feature F-III broadens and shifts towards blue as SiO_2 increases; whilst, the high-frequency (and overlapped) components in the F-III window are progressively more evident as SiO_2 increases (Fig. 2).

In Fig. 3 the individual fitted band components for both Raman (a) and FTIR (b) spectra in all six samples are reported (coloured lines), as well as the total fitted spectrum. The results of the fitting procedure are also reported in Table S1a,b, where the peak parameters of position and FWHM are reported for each of the six samples. Additionally, the normalized peak Area % over the whole 200–1250 cm^{-1} spectrum range and each of the subregion features (F-I for the R, D_1 and D_2 peaks; F-II for X_1 and X_2; F-III for Q^1, Q^2, Q^3 and Q^4) are also reported.

Starting from the Raman spectra, the positions of the most straightforward and discernible peaks in the R_{100} sample, *i.e.* around 450, 800, 1000 and 1100 cm^{-1}, were selected as starting reference positions. In contrast, the band components with less detectable positions were first estimated from the literature (Neuville et al., 2014 and references therein). Again, the bands falling in the same frequency region were constrained to share the same peak width, except the R band in F-I that was modelled with an asymmetric Gaussian band (see below). Three band components are identified in the low frequency region F-I around 415, 480 and 570 cm^{-1}, the F-II intermediate frequency region is reproducible using two bands at 740 and 800 cm^{-1} and the third broad feature at higher frequency region F-III is instead modelled with four bands located close to 940, 1000, 1080 and 1160 cm^{-1} (Fig. 3).

4. Discussion

4.1. Assignment of band components

For the Raman spectra, the assignment of peaks starts from the indications in Neuville et al. (2014) and references therein. In the low frequency region, the three peaks at 415, 480 and 570 cm^{-1} are assigned respectively as R, D_1 and D_2 (Neuville et al., 2014; Drewitt et al., 2022; Cassetta et al., 2023a). The D_1 and D_2 bands are associated with the breathing motions of the Si-O-Si bonds in 4- and 3-membered rings, respectively. At lower frequencies, Si-O-Si vibrations under the R band are likely to be associated with larger rings (≥ 5 tetrahedra) or simply
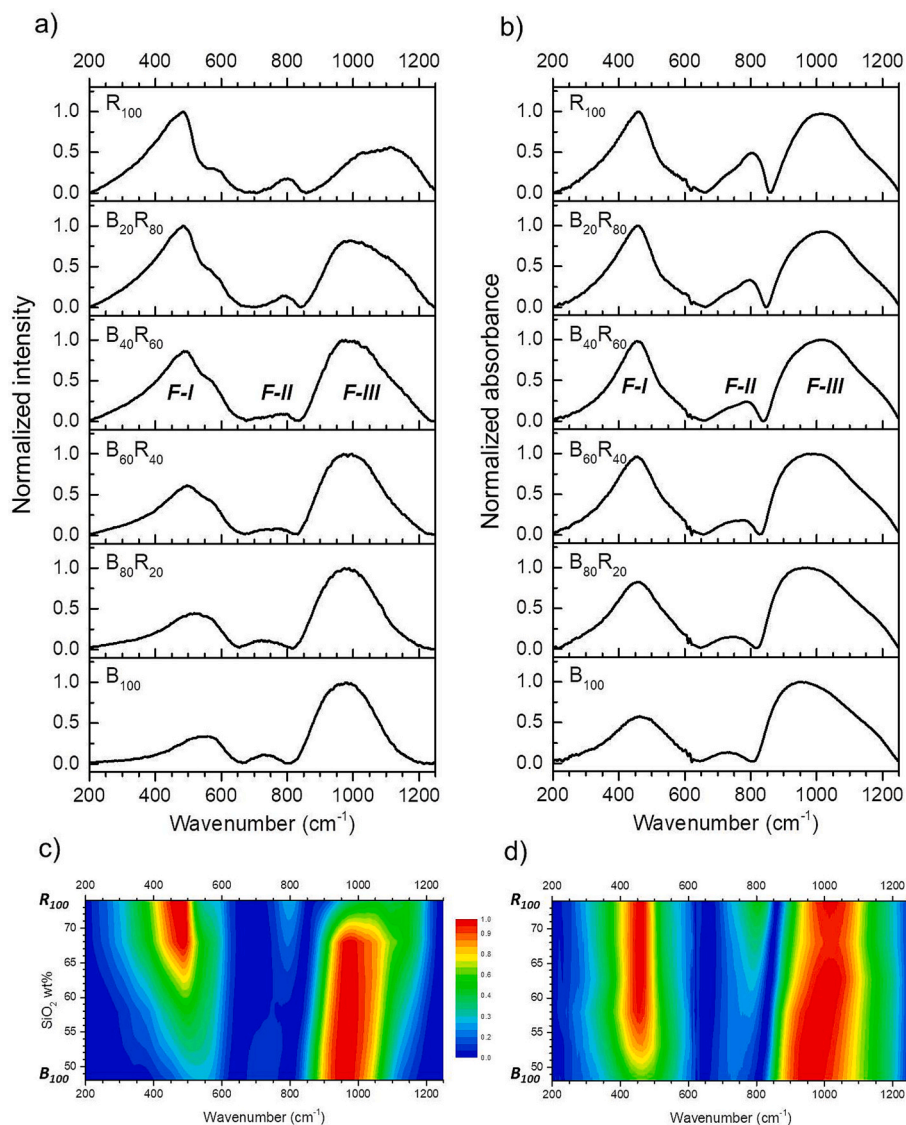
Fig. 2. Processed spectra a) Raman and b) FTIR; heat maps of relative intensities (red is the highest intensity, dark blue the lowest one) for c) Raman and d) FTIR against SiO$_2$ content. (For interpretation of the references to colour in this figure legend, the reader is referred to the web version of this article.)

larger angles of Si-O-Si linkages that may not be associated with ring structures. Unlike the other bands fitted to the Raman spectrum, this band is not symmetric but has a tail to lower frequency (*e.g.* Neuville et al., 2004); this is related to the contributions from progressively less frequent *n*-membered rings and more open Si-O-Si angles and for this reason an asymmetric Gaussian peak was chosen for fitting. The attribution of the two peaks in the intermediate frequency region (labelled here X$_1$ and X$_2$) is still a matter of debate. However, Neuville et al. (2014) and Drewitt et al. (2022) associate the band with stretching vibrations of SiO$_4$ tetrahedra (see also Spiekermann et al., 2013); furthermore, some authors associate these peaks to the motion of Si atoms in its oxygen cage, with a greater atomic displacement of Si compared to O atoms (Mysen et al., 1982; McMillan, 1984).

The interpretation of the features in the high frequency region is also somewhat disputed, but most studies are in general agreement with the Q-speciation fitting proposed by McMillan (1984) and Mysen et al. (1982; 1990). The broad multicomponent set of overlapping peaks is attributed to the convolution of TO$_4$ (T = tetrahedrally coordinated cation) stretching modes. The contribution of the different TO$_4$ units can be extracted by fitting the high frequency region with different Gaussian components, each corresponding to a specific Q^n species, where *n* refers

to the number of bridging oxygens bonded to T, *i.e.* the number of other TO$_4$ groups linked to that particular TO$_4$ unit. The F-III region in our FTIR and Raman spectra can be adequately reproduced using only four Gaussian components. These components may correspond to the Q^1, Q^2, Q^3, and Q^4 species of SiO$_4$ units, with peak positions approximately centred at 850, 900, 1100, and 1150 cm^{-1}, respectively (Mysen et al., 1982; McMillan, 1984; Mysen, 1990; Neuville et al., 2014).

However, the significant presence of aluminium in our glass samples casts doubt on this interpretation. Q^n species of AlO$_4$ units are likely to have lower frequency stretching vibrations compared to the same Q^n species of SiO$_4$ due to their lower bond valence and longer Al-O bond length compared to Si-O (Mysen et al., 1982; McMillan, 1984). Since only four distinct Gaussian shaped bands in the F-III region are resolved here, it cannot be excluded that possible Al-O stretching vibrations are located in the lower frequency portion of this window, in overlapping with the more depolymerized Q^1 and Q^2 species of SiO$_4$ tetrahedra. To a first approximation, we can instead assume that the two bands at the highest frequency, attributed to Q^3 and Q^4 units, are mostly associated with SiO$_4$ tetrahedra.

Moreover, the last spectral window F-III has recently been fitted by as many as 7 Gaussian peaks, mainly encompassing the inspection of the
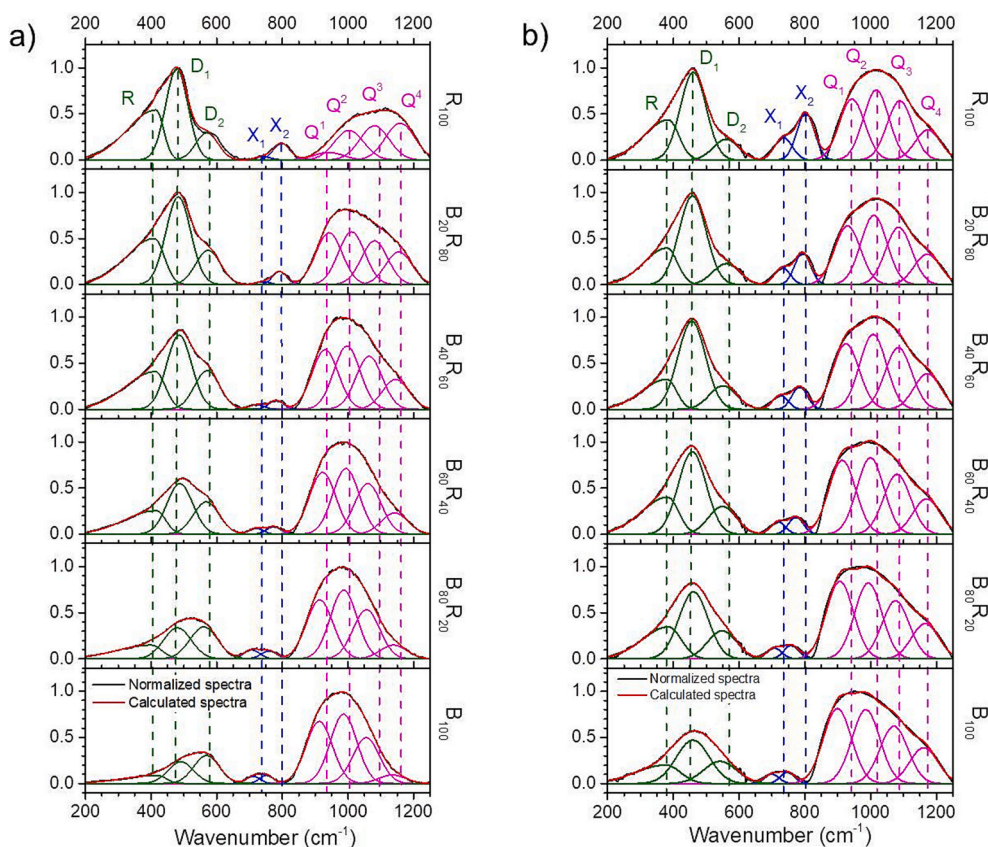
Fig. 3. Fitted bands for the a) Raman and b) FTIR spectra. Fitted bands are in green (F-I), blue (F-II) and cyan (F-III); calculated and measured spectra are in red and black, respectively. Vertical and coloured dashed lines are the peak positions measured for the R_{100} rhyolite glass used as an eye guide. (For interpretation of the references to colour in this figure legend, the reader is referred to the web version of this article.)

high frequency region of polymerized systems (Welsch et al., 2017; Stabile et al., 2021). By contrast, our dataset includes glasses characterized by wide and broad high frequency bells typical of depolymerized basaltic glasses (Cassetta et al., 2022, 2023a). This challenges the clear distinction between customary contributions typically observed in straightforward binary and ternary silicate systems (Le Losq and Neuville, 2013; Le Losq and Neuville, 2017). We overcome this issue by avoiding the splitting protocols for the Q^4 band as indicated in Le Losq and Neuville (2013), as well as for the bimodal distribution of the Q^2 unit (Kilymis et al., 2019). Analogously, we neglected the filtered contribution of the stretching vibrational mode of TO_2 units (T^{2s}) as well as that of the Fe^{3+} band (Welsch et al., 2017; Stabile et al., 2021). This choice is due to the uncertainty in the assignment of the Fe^{3+} band in FTIR spectra and the magnitude and relative intensity with which T^{2s} affect the high frequency region of the Raman and FTIR spectra. However, for the sake of simplicity, we opted to assign a Q^n unit ($n = 1, 2, 3, 4$) to each of the bands, such that the integrated intensity of the band is a relative measure of tetrahedrally coordinated cations with n bridging oxygens, according to the structural model for silicate glasses and melts first adopted by Mysen et al. (1982).

FTIR spectroscopy is an absorption method but has been far less used than Raman for characterizing Q-speciation of natural and chemically complex glasses, except for instance to the Q-structural changes in soda-lime silicate glasses (*e.g.* Biesuz et al., 2023). It follows that vibrational modes associated with specific structural units can be expected to be both Raman and IR active (Herzberg, 1984; McMillan, 1984). This, for example, is more evident in the F-II region where both spectra show the presence of two peaks at similar frequencies, also having similar relative integrated intensities for each sample. These observations justify the application of the same fitting strategy for both FTIR and Raman data.

4.2. Similarities and differences between the Raman and FTIR spectra

One of the major aims of this work is to highlight similarities and differences between the Raman and FTIR spectra on a series of glasses with sub-alkaline chemical signatures. It should be noted that these compositions are the most abundant on Earth and many other planetary bodies (Vetere et al., 2015, 2017; Vetere et al., 2019; Pisello et al., 2019; Sehlke and Whittington, 2015). This comparison reveals similar features between the two techniques and justifies applying a common fitting strategy (Figs. 1S, 2S, 2 and 3). Thereby, the pre-fitting and fitting strategy adopted here for both Raman and/or FTIR spectra can be considered in future applications aimed to unravel the SRO-structures of other natural multicomponent silicate glasses (see TAS in Fig. 1). The salient differences between the two probing methods are displayed in Fig. 4. Most of the normalized abundances from the three frequency windows (F-I, F-II, and F-III) and the nine individual band components (depicted in Fig. 3) obtained by Raman and FTIR analysis, closely align along a 1:1 relationship with some exceptions (Fig. 4). The closest similarities in area% of single band components are displayed by the intermediate $B_{60}R_{40}$ glass, followed by that for $B_{40}R_{60}$ (except X_1 and X_2), whereas greater differences are progressively observed for the glasses with compositions closer to those of the two end-members; the R_{100} shows the most pronounced differences (Fig. 4a). This behaviour probably suggests that spectroscopic features of the two end-members glasses could be more affected by background and/or fitting procedure than the intermediate compositions.

The examination of the evolution of the single bands may be further extended by considering the area% tot of the three main features (F-I, F-II and F-III in Fig. 4b). From these comparisons it is evident that the X_1 and X_2 band components in the F-II spectral window are better resolved by FTIR than Raman, although their integrated intensities are always
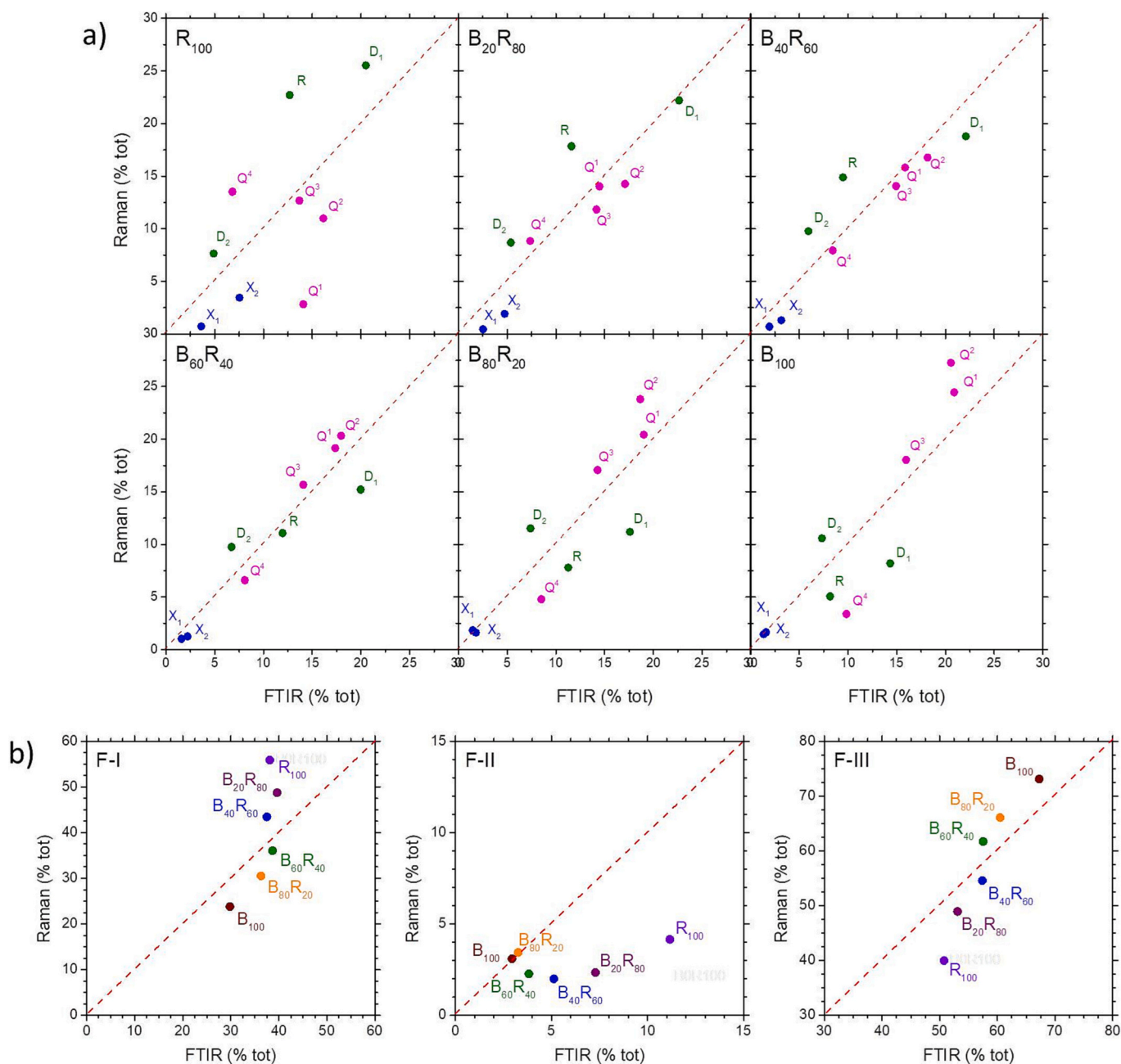
Fig. 4. Comparison between the normalized abundances (area % tot) of band components obtained *via* Raman and FTIR analysis in the six studied samples for the nine fitted band components (a) and (b) of the whole features F-I (3 band components), F-II (2 band components) and F-III (4 band components).

relatively low. This implies that FTIR is more suitable to probe the evolution of these two bands as a function of chemical composition (Fig. 4b). By contrast, the components in the F-I region of the $B_{40}R_{60}$, $B_{20}R_{80}$ and R_{100} glasses are progressively more intense (area% tot) when analysed by Raman and $B_{60}R_{40}$, $B_{80}R_{20}$ and B_{100} when recorded by FTIR (Fig. 4b). A similar but inverse situation holds for the F-III region (Fig. 4b).

In Fig. 5 the differences between the positions of the fitted peaks in FTIR *vs* Raman spectra are reported for the six glasses. The positions of components in the FTIR spectra are always found at lower frequencies (negative quadrant) in the F-I region, with differences of −10 to −45 cm^{-1} compared to Raman; in F-II the differences are much smaller, between −10 and + 5 cm^{-1} (Fig. 5). Regarding F-III, the differences in frequencies are about −7, +6, +14 and + 24 cm^{-1} for Q^1, Q^2, Q^3 and Q^4, respectively (Fig. 5).

These differences in band intensities (Fig. 4a) and positions (Fig. 5) can be either attributed to a) cross section, where a mode is more visible (*i.e.* active) if probed with one technique compared to another (*e.g.* Ferraro et al., 2003), or b) to the intrinsic errors of the selected fitting methodology as a consequence of background modelling, band overlap, actual number of active bands, positions and width (FWHM). The lowest frequency R and D_1 bands, as well as the highest-frequency Q^4 band, display the greatest differences in both position and area% of the total spectrum between Raman and FTIR (Figs. 4a and 5). Interestingly, it is evident from Fig. 5 that the differences in peak positions observed are frequency dependent in the case of each sample and that this dependence is influenced by chemical composition; in turn, the slope of the trend increases with increasing basaltic content. This is indeed related to the still limited knowledge of the actual number and associated features of bands.
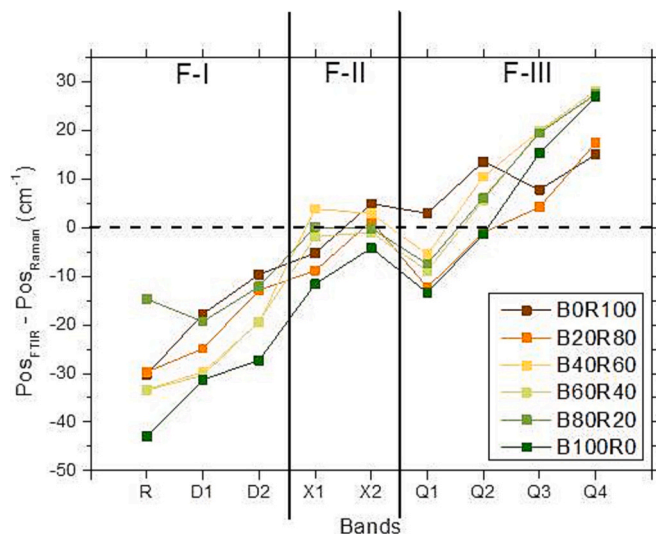
Fig. 5. Differences in fitted positions between peaks in the FTIR and the Raman spectra as a function of the composition of glasses.

At the same time, these observed differences are also related to more evident variations between F-I and F-III in Raman than in FTIR (Fig. 2). Likewise, F-II bands display higher intensities in FTIR compared to

Raman (Fig. 2). These differences are evident when the samples are compared by area% in the three subregions F-I, F-II and F-III especially for the glasses with or close to the end-member compositions (Tables S1a and S1b, Fig. 4). On the whole and under the reported analytical conditions, Raman spectroscopy highlights more markedly the integrated intensities of the R, D_1, D_2 breathing modes in F-I where they show greater variability ($\Delta\%_{tot} \sim 30\%$) between the two end-members compared to FTIR results ($\Delta\%_{tot} \sim 10\%$). Also, variability among the Q^n stretching modes in F-III is about 35% and 20% for Raman and FTIR respectively. Conversely, FTIR spectra present a variability four times greater ($\Delta\%_{tot} \sim 8\%$) for the X_1 and X_2 F-II intensities compared to Raman ($\Delta\%_{tot} \sim 2\%$). Additionally, Fig. 5 suggests that using this analytical approach the X_1 and X_2 peaks are equally represented by both Raman and FTIR. This highlights the crucial advantage of focusing on particular spectroscopic ranges that can reveal important information on sub-alkaline glasses regardless of the spectroscopic technique used (Pisello et al., 2019).

4.3. Correlations between composition and spectral features

A further goal of this work is to relate the vibrational features from both spectroscopic methods to the chemical systems evolving along the substitutional join between basalt and rhyolite. This allows us to retrieve chemical and structural information from glasses by on-field analysis (Schröder et al., 2020) or collected by planetary facilities and rovers (Bandfield, 2002; Rull et al., 2017). In Fig. 6a, b and c the fitted
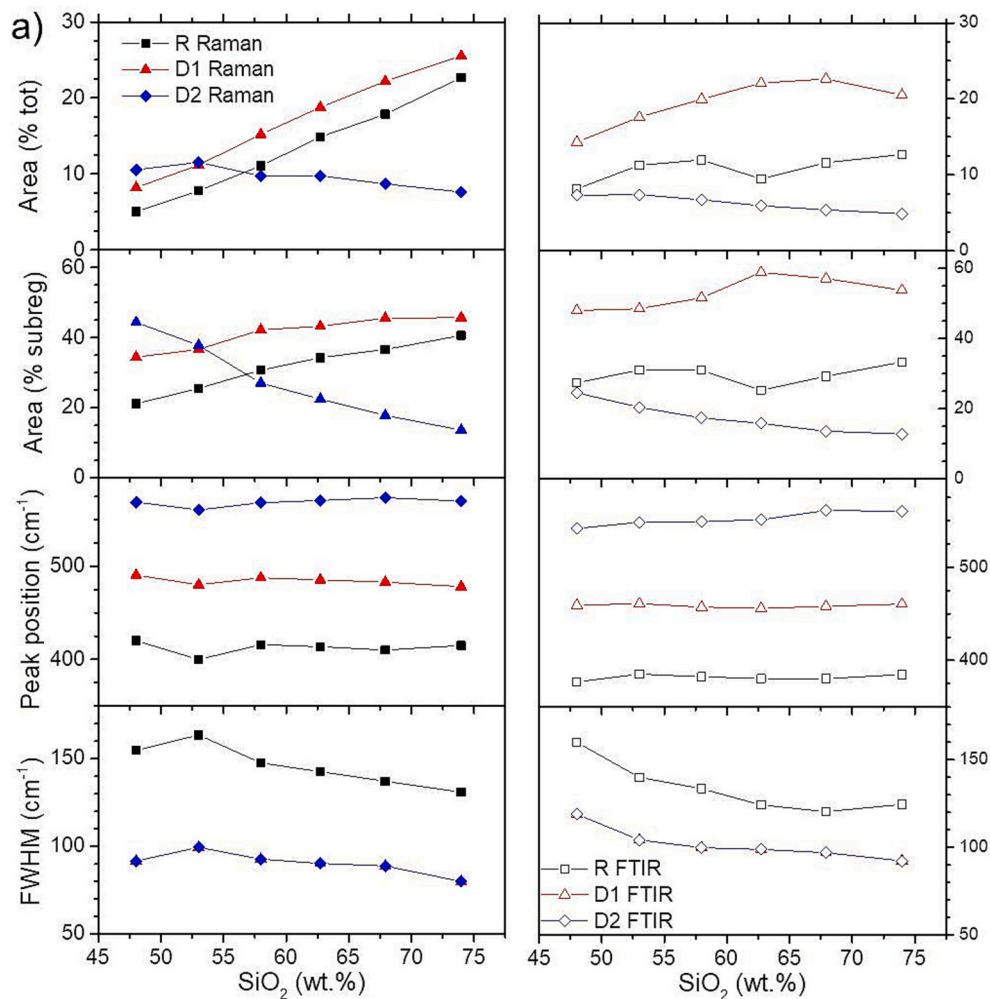

Fig. 6. Raman (left) *vs* FTIR (right) fitted peak parameters in the F-I low frequency region (a), in the F-II intermediate frequency region (b) and in the F-III high frequency region (c).
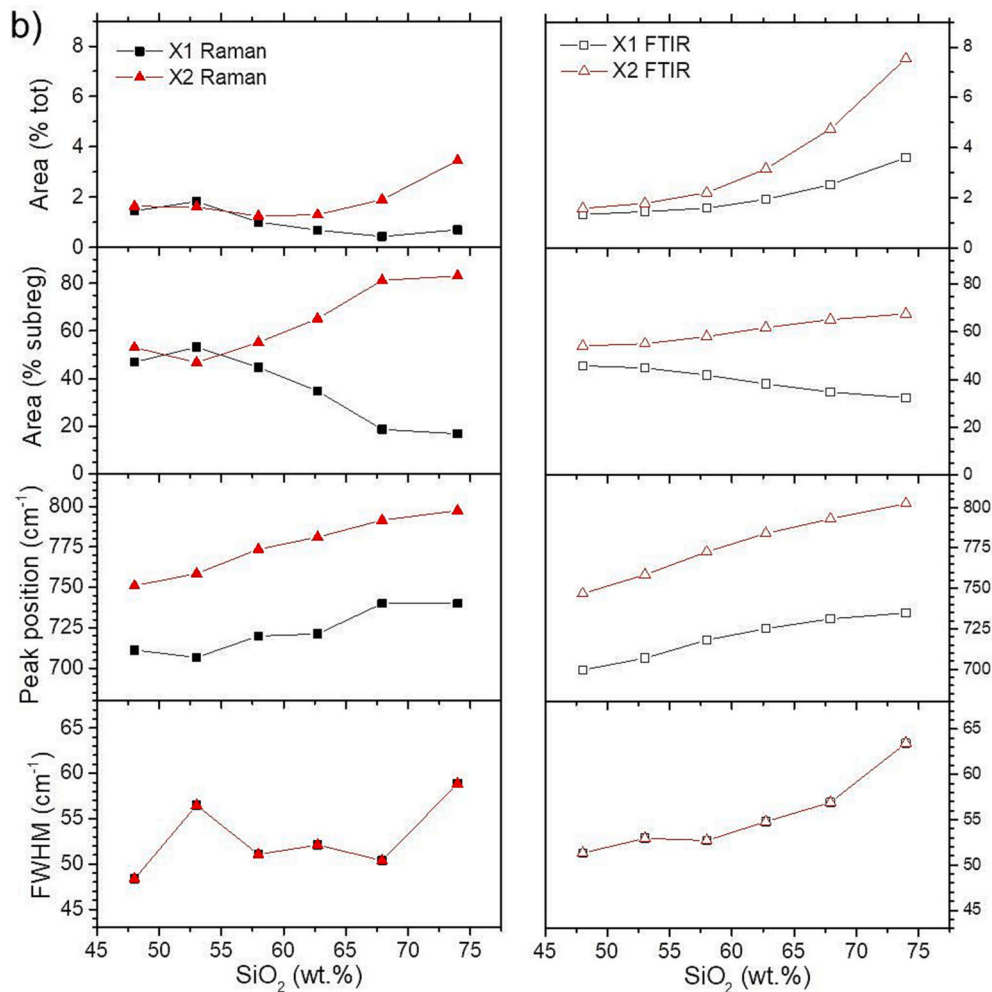
Fig. 6. (*continued*).

parameters are plotted against the SiO_2 content, the most abundant and characterizing chemical component. As SiO_2 content increases, both the Raman and FTIR peak positions of the R, D_1 and D_2 bands remain nearly constant; their widths substantially decrease, but the intensities of both the R and D_1 peaks increase at the expense of the D_2 band intensity; these latter variations are more linear and marked in the Raman spectra (Fig. 6a). In turn, SiO_2-rich glasses (rhyolite and dacite) are characterized by smaller FWHM and notably larger R and D_1 band intensities (Fig. 6a).

Inspection of the F-II spectral window, albeit less intense than the other two features (Figs. 2, 3), allows us to tightly relate the evolution of the X_1 and X_2 bands with the bulk chemistry (Fig. 6b) for both Raman and even to a greater extent for the FTIR spectra. Their peak positions and intensities within the spectral subregion (area% subreg.) follow monotonic, linear and increasing trends as SiO_2 increases (Fig. 6b). In summary, the progressive blue-shift of both X_1 and X_2 bands coupled with the mutual increasing intensity of X_2 at the expense of X_1 can be used to measure the SiO_2 content in these glasses quantitatively. Although they are weak in intensity, these features display the most quantitative, straightforward, and easy-to-measure correlations to chemical composition, especially in the case of FTIR spectroscopy (Fig. 6b).

The trends for the Q^n species as SiO_2 content increases are reported in Fig. 6c. In this F-III region, the bands strongly overlap (Figs. 2, 3) and the widths of bands are insensitive to position along the compositional join. Peak positions, however, show parallel trends for all four bands, increasing smoothly as a function of SiO_2 content, indicating relatively

stronger Si-O bonds for each Q-species in glasses with increasing rhyolitic component. This behaviour can be rationalized by the decreasing average field strength of network modifying cations along the join as $(Na + K)/(MgO + CaO)$ increases exponentially with increasing SiO_2. Integrated intensities of the bands in the F-III region are much more dependent on chemical composition and can be considered an even more effective means of describing the overall degree of polymerization of the glass *via* Q-speciation.

The Raman spectra display more pronounced trends in peak areas (in particular Q^1 and Q^4) than FTIR as a function of SiO_2 content (Fig. 6c). Nonetheless, the chemistry of the glass is more directly mirrored by the shifting of the Q^1 species compared to Q^4 species (30–40 cm^{-1} *vs* 10–20 cm^{-1}). In detail, the local Raman intensities (area% subreg.) change almost linearly from basalt to dacite glasses, showing a progressive decrease of Q^1 and Q^2. In contrast, the Q^3 band remains nearly constant and Q^4 species markedly increases (Fig. 6c). As the composition shifts from dacite to rhyolite one observes a drastic decrease in the Q^1 component (close to 5 area %) and a steeper increase in the Q^3 and Q^4 band intensities (Fig. 6c). In synthesis, integrated intensities are ordered as $Q^2 > Q^1 > Q^3 > Q^4$ from basalt (B_{100}) to dacite ($B_{20}R_{80}$) and then as $Q^4 > Q^3 > Q^2 > Q^1$ from dacite to rhyolite (R_{100}). The evolution of intensities of Q species by FTIR is less marked than Raman and only Q^1 displays a slight but roughly monotonic decreasing trend (Fig. 6c), albeit the Q^1 is rare even in the B_{100} bulk system (Henderson et al., 2006). This effect may be attributed to two main factors: i) trade-offs from baseline modelling and ii) the overlapping with IR strong modes such as the anti-symmetric stretching mode of the TO_4 units located around 1050 cm^{-1}
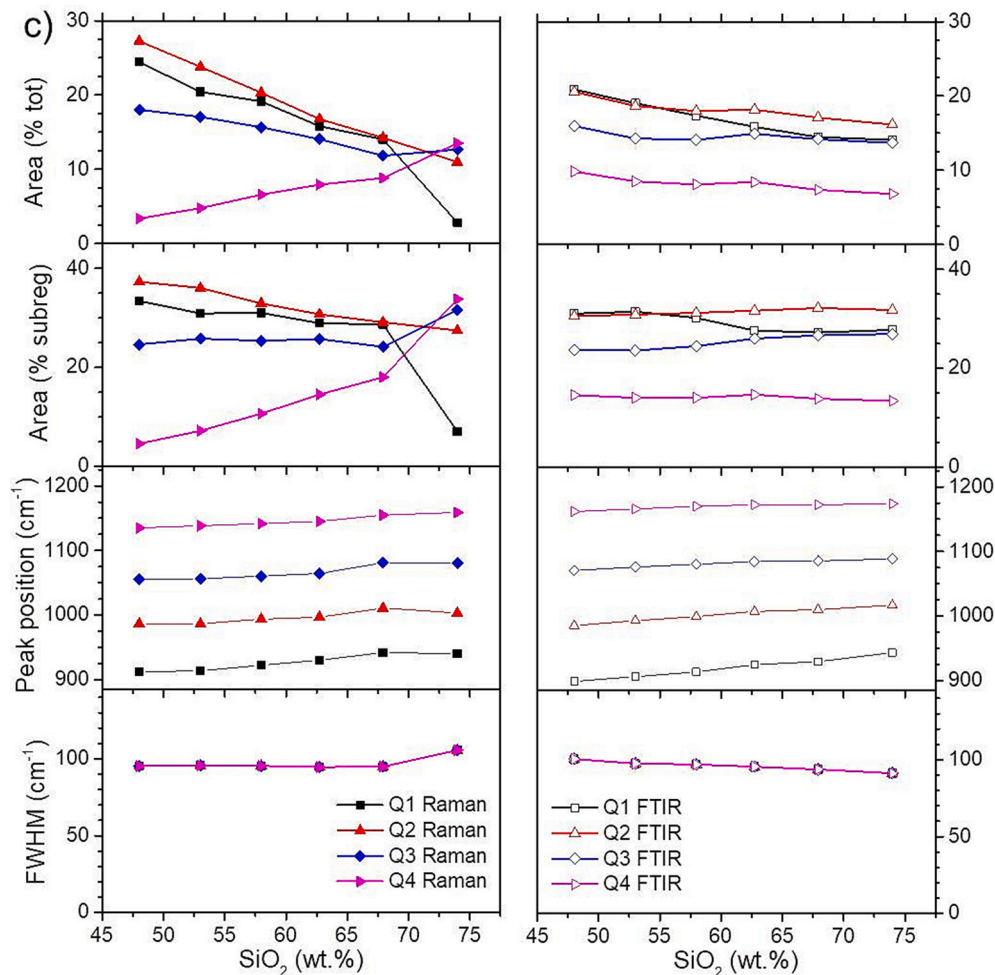
Fig. 6. (*continued*).

(*e.g.* Gunde, 2000).

The variation of these vibrational parameters draws an interesting picture of the evolution of the silicate short range order (local molecular arrangement) along this natural and chemically complex substitutional join. This approach and related outcomes complement, refine and extend conclusions achieved by many previous studies commonly focused on more simplified systems (*e.g.* Mysen, 1990; Neuville, 2006; Neuville et al., 2006; Le Losq and Neuville, 2013; Di Genova et al., 2015, 2017). Moving from this state of the art, we further stress some aspects of the local atomic arrangements (SRO). A common praxis is to consider the elements based on the interaction with the tetrahedral network, *i.e.* in terms of network formers, intermediates and modifiers (Maekawa et al., 1991; Mysen and Richet, 2005; Neuville et al., 2022). In Fig. 7 the compositions (in terms of wt%) of the six glass samples are rearranged in terms of the system network former-intermediate-modifier, such as network formers are SiO_2, P_2O_5, intermediates are TiO_2, Al_2O_3 and Fe_2O_3 and modifiers are the remaining oxides. Fe_2O_3 and FeO abundances were calculated after Vetere et al., 2015. As expected, the rhyolite glass (R_{100}) mainly consists of network formers (> 73 wt%), while the basalt sample (B_{100}) is relatively richer in modifiers (29 wt%) and intermediates (23 wt%; Table 1). In terms of network structure, this evolution translates into changes in the glass structure as highlighted by the three spectral features both in the Raman and FTIR spectra. Depolymerisation, induced by the addition of network modifiers, appears to have a greater effect at reducing the overall intensity of the F-I region, where we can expect atomic vibrations involving bridging oxygens (see Figs. 2c,d). Among the three fitted bands in the low frequency region,
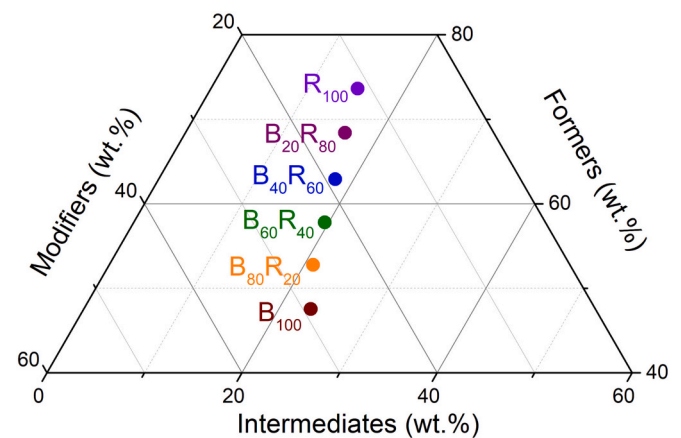

Fig. 7. Glass composition in the ternary system network former-intermediate-modifiers. Network formers are SiO_2 and P_2O_5; intermediates are TiO_2, Al_2O_3 and Fe_2O_3 and modifiers are the remaining oxides. Fe_2O_3 and FeO abundances were calculated by Vetere et al. (2015).

the D_2 band appears to be least sensitive to changes in the degree of polymerization, suggesting that more open Si-O-Si angles are subject to breaking with the addition of network modifying cations.

An additional effect correlated to the increase in network formers is the change in the relative abundance of Q^n species. Theoretically, in pure silica glass only Q^4 species are present and the abundance of this

species rapidly decreases as network modifiers are added (Dupree et al., 1984; Neuville et al., 2014), leading to the formation of tetrahedral cation species with an increasing number of non-bridging oxygens (NBO). Calculated NBO/T values for our glasses do not exceed 0.53 (basaltic endmember glass) suggesting that overwhelming abundances of Q^3 and Q^4 should be present in all of our glasses (50% Q^3 + 50% Q^4 would result in NBO/T = 0.5). To a first approximation, we have assumed that the changes in SRO related to Q-speciation along this compositional join are dominated by a simple shift in the ratio of Q^3/(Q^3 + Q^4), evidenced by the linear relationship that we observe between integrated peak area Q^3/(Q^3 + Q^4) and NBO/T (see below). These two peaks have been commonly assigned to Q^3 and Q^4 units in numerous Raman studies of simpler two- or three-component silicate glasses (*e.g.* Neuville et al., 2014). Nonetheless, additional peaks in the lower frequency portion of the F-III region of both spectra are observable and their intensities also vary as a function of composition. At the same time, they could be attributed to more depolymerized Q-species (Q^1, Q^2) as has been suggested in studies of more depolymerized silicate glasses (Kalampounias et al., 2009; Le Losq and Sossi, 2023).

The bands near 900 and 1000 cm^{-1} may also be associated with the stretching vibrations of AlO_4 tetrahedra. Their frequencies should be lower than the same Q^n-species of SiO_4 tetrahedra due to their weaker bond valence and longer T-O bond length. For example, the increasing area% of the Q^1 and Q^2 bands as composition becomes more basaltic could be due to the increasing contribution of Al-O stretching vibrations compared to Si-O stretching vibrations as the Al_2O_3/SiO_2 ratio increases from 13.48/73.97 (R_{100}) to 15.59/48.02 (B_{100}) wt%. The intensities of these bands may also be enhanced by the overlapping Q^3 and Q^4 Al-bearing species, which may have lower frequency stretching modes compared to Si-bearing Q^3 and Q^4 species (King et al., 2004). For the studied compositions, isolated tetrahedral structures or Q^0 species, usually located below 900 cm^{-1} (Moulton and Henderson, 2021; Neuville et al., 2022; Cassetta et al., 2024), are not expected in line with the fitted components (Fig. 3). According to Raman results (Fig. 5), the addition of network modifier oxides replacing SiO_2 is associated to a marked and progressive decrease of the relative abundance of the Q^4 species and less markedly Q^3. A major increase can be observed in the Q^1 molecular unit, while that for Q^2 remains relatively constant. These variations are less marked in the FTIR spectra: the titular increase in the relative abundance of the Q^1 cluster is mirrored by the decrease of Q^3, while both Q^2 and, most notably, Q^4 are unchanged (Figs. 3, 6c).

The role of iron in such systems deserves particular attention since it is observed in both of its valence states Fe^{3+} and Fe^{2+}, due to both the redox conditions applied (Farges et al., 2004) and the surrounding chemical environment (Borisov et al., 2017; Di Genova et al., 2018; Cassetta et al., 2023b). For instance, alkalis tend to have a greater stabilizing effect of Fe^{3+} compared to alkaline earth cations. K_2O-rich glasses have the highest ferric iron contents under the same oxygen fugacity compared to K_2O-poor glasses. In addition, although less important than alkalis, the role of CaO appears to have a moderate but not insignificant impact on the increase in ferric iron (Borisov et al., 2017). Another explanation can be inferred by examining structural evolution as a function of concentration and relative proportion of K^+ and Na^+. Compared to large-membered rings, the percentage of small-membered (three, four) rings is larger in K-rich glasses than in Na-rich glasses. Additionally, both the mean T-O-T angle and force constant increase when K^+ grows at the expense of Na^+ (Le Losq and Neuville, 2013). Both effects can also be accompanied by a dramatic decrease in the Q^1 area, as well as by increases in both Q^3 and Q^4 species. The transition from dacite to rhyolite encompasses a substantial depletion of Ca^{2+} and Mg^{2+} accompanied by an increase of about 20% of K^+ (representing the dominant alkaline phase). From the iron coordination state perspective, it could facilitate the shift from modifier to former with a greater magnitude together with a K-induced network stiffness (Di Genova et al., 2017; Onodera et al., 2019).

Although a proper assignment of the bands in the intermediate feature F-II is still debatable, from the evolution of these bands it is still possible to derive the evolution of the short-range structure. Two different but clear trends moving from basaltic to rhyolitic compositions are detected: an increase in the intensity of the X_2 peak at the expense of the X_1 peak and the shift of both peaks to higher frequencies together with a progressive broadening (Fig. 4b). It is remarkable that, in contrast to the other two features F-I and F-III, these trends are less evident in Raman spectra compared to FTIR spectra (Figs. 2, 3 and 6c). Due to the similar, but somehow antithetic, behaviour of these two peaks we can associate them to the same vibrational mode of two different environments. The evolution of peak intensities in Fig. 6b in regard to chemistry changes (Table 1) suggests that the X_2 peak may be associated with an environment of Si-centred tetrahedral sites, whereas the X_1 peak indicates an environment of Al-centred tetrahedral sites. More broadly, the integrated peak intensity of X_2 is also correlated to the abundance of network formers while that for X_1 to network intermediates. The overall decrease in network modifiers moving to rhyolite compositions is also mirrored by the blue shift of the X_1 and X_2 peak position that testifies to an increase in the bond strength of the tetrahedral sites (*e.g.* Ferraro et al., 2003).

4.4. Identifying sub-alkaline glass using vibrational spectroscopy

The extreme chemical variability of the glass samples analysed in this work is both a strength and a weakness. On the one hand, it is possible to observe a synthesis of the spectral evolution of the most abundant volcanic glasses on Earth. On the other hand, the extreme variability of oxide concentrations involved does not allow us to map out their impact on the spectra in finer detail. In detail, each sub-region of the measured spectra contains diagnostic features. By crossing these clues it could be possible to retrieve the type of glass exclusively from the spectroscopic fingerprint. In Fig. 8, the most significant correlations relating to spectroscopy and chemistry for each subregion are selected along with the sub-alkaline glass ranges according to the TAS diagram. In Table 2, the regression equations are reported as linear correlations: $y = m \bullet x + q$, where x is the diagnostic parameter considered in each region and y is SiO_2 (wt%) or NBO/T. Obviously, these last two parameters are strongly correlated with the samples analysed in this work (R^2 > 0.99).

Considering the overall trend of the intensities of the three identified features in the spectral region (Fig. 2), one can observe a consistent rise in the intensity of the entire F-I feature as the SiO_2% (wt%) content increases. In Fig. 8 (top graph) the intensity of the F-I feature over the total processed spectrum (*i.e.* F-I + F-II + F-III) is plotted against SiO_2 content (wt%) for both Raman and FTIR. The results from Raman show an astonishing positive correlation (R^2 > 0.99%) with chemistry (Table 2). In contrast, the FTIR results show a similar intensity increase for SiO_2-poor compositions followed by a flat trend in SiO_2-rich glasses. As expressed in the previous paragraph, this trend is associated with the increasing frequency of larger and more complex tetrahedral structures, defined by the R and D_1 peaks, moving to rhyolite-like compositions.

This aspect may be tracked in depth by focusing on the F-I subregion that reveals a powerful diagnostic feature in the intensity trends registered, this time, in both Raman and FTIR spectra. As stated earlier, the SiO_2 increase is marked by a progressive increase in the intensities of the R and D_1 bands relative to the D_2 band (Fig. 6a, area% subreg.). The strong correlation between the SiO_2 content and the ratio between the band associated with 3-membered ring structures (D_2) and larger linked tetrahedral structures (R and D_1) is displayed in Fig. 8 (second from the top). This strong correlation (as reported in Table 2) can be observed in both Raman and FTIR spectra. The differences in the regression parameters are attributed to the different sensibilities of the chosen methodology to probe this spectrum region (as already observed in Figs. 4 and 6a), with Raman presenting a more robust and consistent R^2 value than FTIR. Interestingly, the difference in the (R + D_1)/(R + D_1 + D_2) ratio between the two techniques is larger for the basalt glass and non-existent for rhyolite. Conversely, the position of the X_2 band is the
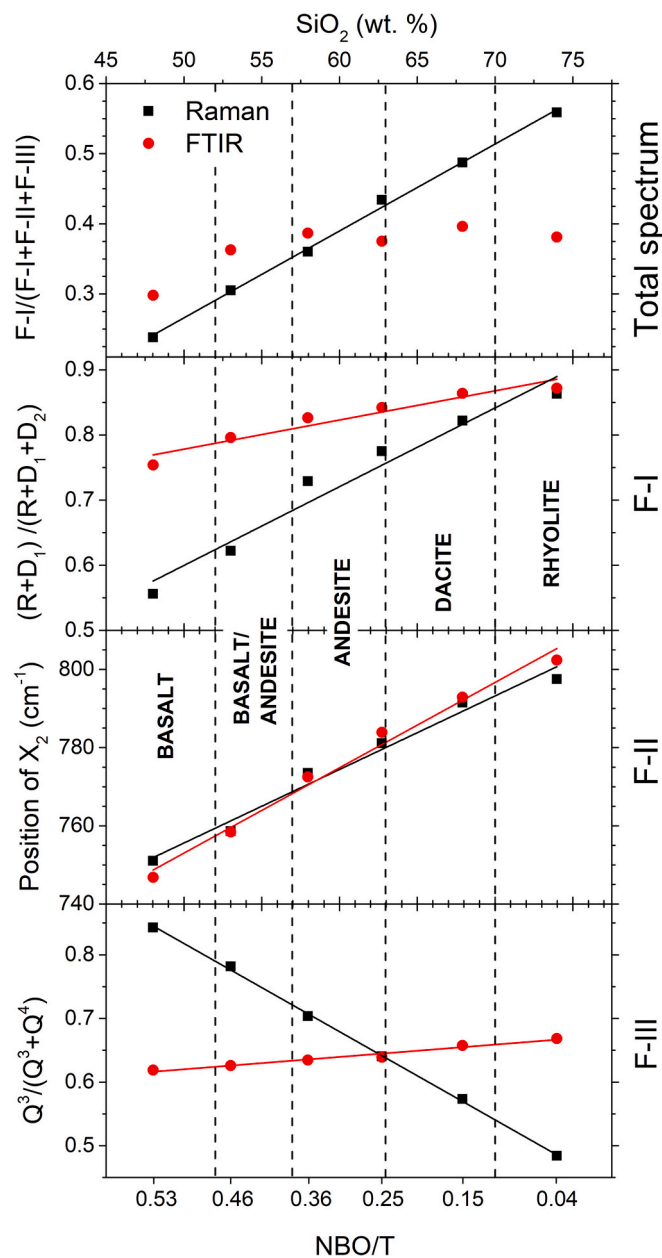
Fig. 8. Correlation between the extracted fitting parameters and the SiO$_2$ (wt %) and NBO/T contents of the six studied samples. All parameters refer to the band area normalized in the subregion (area% subreg.) except for the X$_2$ band where positions are reported. Additionally, the sub-alkaline glass ranges according to the TAS diagram are also reported; the limit between the dacite and the rhyolite field was set at 70% SiO$_2$ close to the trachyte-dacite-rhyolite junction. Solid lines are regressions with fitting parameters reported in Table 2.

superior diagnostic feature for the F-II region Fig. 6b. In Fig. 8 (third from the top) the position of the fitted peaks *vs* the SiO$_2$ content for both techniques is reported. Significantly, the fitted values for Raman and FTIR exhibit a high degree of overlap, and their regression values (Table 2) are remarkably similar. This confirms that both techniques can be reliably employed to explore this specific spectrum region. The similarities of the evolution of these components in FTIR and Raman spectra are likely associated with the fact that there is lesser uncertainty in background subtraction and also a lesser degree of peak overlap in this subregion of the spectra (Fig. 3). In contrast, the few but significant differences observed in the other two (F-I and F-III) regions (Fig. 6a) could be partly attributed to greater uncertainties regarding the actual

Table 2
Regression parameters for selected linear relationships are reported in Fig. 8.

Spectroscopy	Subregion	Relationship	Slope (m)	Intercept (q)	R^2
Raman	Total	SiO$_2$ *vs* F-I/(F-I + F-II + F-III)	0.81 ± 0.02	28.6 ± 0.8	>0.99
		NBO/T *vs* F-I/(F-I + F-II + F-III)	0.0016 ± 0.0002	0.579 ± 0.007	0.94
	F-I	SiO$_2$ *vs* (R + D$_1$)/(R + D$_1$ + D$_2$)	79 ± 8	3 ± 6	0.95
		NBO/T *vs* (R + D$_1$)/(R + D$_1$ + D$_2$)	−1.5 ± 0.2	1.4 ± 0.1	0.94
	F-II	SiO$_2$ *vs* Position of X$_2$	0.52 ± 0.04	−343 ± 29	0.97
		NBO/T *vs* Position of X$_2$	−0.0102 ± 0.0007	8.2 ± 0.6	0.97
	F-III	SiO$_2$ *vs* Q^3/(Q^3 + Q^4)	−72 ± 1	109.0 ± 0.7	>0.99
		NBO/T *vs* Q^3/(Q^3 + Q^4)	1.40 ± 0.04	−0.64 ± 0.03	>0.99
FTIR	Total	SiO$_2$ *vs* F-I/(F-I + F-II + F-III)	–	–	–
		NBO/T *vs* F-I/(F-I + F-II + F-III)	–	–	–
	F-I	SiO$_2$ *vs* (R + D$_1$)/(R + D$_1$ + D$_2$)	208 ± 28	−111 ± 23	0.92
		NBO/T *vs* (R + D$_1$)/(R + D$_1$ + D$_2$)	−4.0 ± 0.6	3.6 ± 0.5	0.90
	F-II	SiO$_2$ *vs* Position of X$_2$	0.45 ± 0.03	−290 ± 20	0.98
		NBO/T *vs* Position of X$_2$	−0.0088 ± 0.0006	8.2 ± 0.6	0.98
	F-III	SiO$_2$ *vs* Q^3/(Q^3 + Q^4)	–	–	–
		NBO/T *vs* Q^3/(Q^3 + Q^4)	–	–	–

Footnotes: all parameters refer to the band area normalized in the subregion (area% subreg.) except for the total area (in % tot) and position of the X$_2$ band (in cm^{-1}).

number of bands, their positions, shapes and widths.

As described in the previous paragraph, in the third region (F-III) the relationship between the intensity of the Q^3 and Q^4 bands can also be used to describe the SRO as the calculated NBO/T slightly exceeds 0.5. In Fig. 8 (bottom) the intensities (expressed as area% subreg.) of Q^3 over the sum of Q^3 and Q^4 for Raman show a strong inverse correlation (with R^2 over 0.99, Table 2) moving from basalt to rhyolite. Intriguingly, the trend observed in the FTIR spectra is the opposite. Although the correlation is still very good, this behaviour is discordant with the general model of silicate melt polymerization *via* Q-speciation. This discrepancy might also be attributed to the fitting procedure, which appears less suitable for accurately investigating this particular range of the FTIR spectrum.

The correlations presented in Fig. 8 and Table 2 reinforce the conclusions discussed and illustrated by Fig. 4 and further extend them by suggesting that both spectroscopic techniques can, to a reasonable extent, provide valuable chemical insights into the sub-alkaline glass series. However, a notable exception arises in the Q^n region (F-III) of the FTIR spectra, where the baseline subtraction and superimposition of infrared stronger modes significantly impact the expected outcomes (as depicted in Fig. 8, both top and bottom). This effect is particularly pronounced for compositions rich in SiO$_2$, where the higher frequency bands dominate.

5. Conclusions and outlooks

The main achievements of this work can be summarized by the following five points:

1) Raman and FTIR spectra obtained on the six glasses investigated, with composition continuously shifted along the basalt to rhyolite sub-alkaline join, display similar and complementary band features.
2) All spectra can be fitted and adequately reproduced by a compounded linear baseline subtraction and fitted with nine components, divided into three subregions at low-, intermediate- and high-frequencies (F-I, F-II and F-III).
3) Raman and IR relative integrated peak intensities of these components are extremely similar for intermediate glass compositions, but for the basalt and rhyolite end-members several of these components show significant differences in intensity.
4) The intermediate frequency region shows two bands in both spectroscopic methods that are both relatively weak in intensity but their positions are easily measurable and strongly correlate with the bulk composition of glasses, especially in the case of FTIR.
5) The progressive shifting of some band positions and integrated intensities as a function of SiO_2 represents a quantitative chemical proxy to measure the type of glasses in planetary and extra-planetary bodies.

CRediT authorship contribution statement

Francesco Radica: Conceptualization, Data curation, Methodology, Writing – original draft, Writing – review & editing. **Michele Cassetta:** Data curation, Formal analysis, Validation, Writing – original draft, Writing – review & editing. **Gianluca Iezzi:** Conceptualization, Funding acquisition, Project administration, Supervision, Validation, Writing – original draft, Writing – review & editing. **Alessandro Pisello:** Formal analysis, Methodology, Writing – original draft. **Francesco Vetere:** Funding acquisition, Project administration, Supervision, Writing – original draft. **Alessandro Del Vecchio:** Conceptualization, Data curation, Investigation. **Mariangela Cestelli Guidi:** Data curation, Investigation, Supervision. **Brent T. Poe:** Conceptualization, Project administration, Supervision, Writing – original draft.

Declaration of competing interest

The authors declare the following financial interests/personal relationships which may be considered as potential competing interests:

Gianluca Iezzi reports financial support was provided by Gabriele d'Annunzio University of Chieti and Pescara. Francesco Vetere reports financial support was provided by University of Siena.

Data availability

Data are available through Mendeley Data at http://doi.org/10.17632/vdytrvkysc.1.

References

Bandfield, J.L., 2002. Global mineral distributions on Mars. J. Geophys. Res. Planets 107 (6).

Beran, A., Libowitzky, E., 2004. Spectroscopic Methods in Mineralogy, EMU notes in Mineralogy, Vol. 6. Mineralogical Society of America, Chantilly i-xiv + 662 pages. ISBN 963 463 6624.

Biesuz, M., Mariotto, G., Cassetta, M., Ersen, O., Ihiawakrim, D., Haušild, P., Giopato, P., Martucci, A., Bortolotti, M., Sglavo, V.M., Sorarù, G.D., 2023. Solid-state field-assisted ion exchange (Ag → Na) in soda–lime float glass: tin versus air side. Adv. Eng. Mater. 2201572.

Borisov, A., Behrens, H., Holtz, F., 2017. Effects of strong network modifiers on Fe3+/Fe2+ in silicate melts: an experimental study. Contrib. Mineral. Petrol. 172 (34).

Calas, G., Henderson, G.S., Stebbins, J.F., 2006. Glasses and melts: linking geochemistry and materials science. Elements 2 (5), 265–268. https://doi.org/10.2113/gselements.2.5.265.

Cassetta, M., Di Genova, D., Zanatta, M., Boffa Ballaran, T., Kurnosov, A., Giarola, M., Mariotto, G., 2021. Estimating the viscosity of volcanic melts from the vibrational properties of their parental glasses. Sci. Rep. 11 (1), 1–14.

Cassetta, M., Zanatta, M., Biesuz, M., Giarola, M., Mariotto, G., 2022. New insights about the role of Na–K ratio on the vibrational dynamics of synthetic-basalt glasses. J. Raman Spectrosc. 53, 540–549.

Cassetta, M., Giannetta, B., Enrichi, F., Zaccone, C., Mariotto, G., Giarola, M., Nodari, L., Zanatta, M., Daldosso, N., 2023a. Effect of the alkali vs iron ratio on glass transition temperature and vibrational properties of synthetic basalt-like glasses. Spectrochim. Acta - A: Mol. Biomol. Spectrosc. 293 (February), 122430.

Cassetta, M., Vetere, F., Zanatta, M., Perugini, D., Alvaro, M., Giannetta, B., Zaccone, C., Daldosso, N., 2023b. Micro-Raman spectroscopy for a comprehensive understanding of the structural evolution of Basaltic-Andesite and Trachybasalt multiphase systems. Chem. Geol. 616, 121241.

Cassetta, M., Rossi, B., Mazzoccato, S., Vetere, F., Iezzi, G., Pisello, A., Zanatta, M., Daldosso, N., Giarola, M., Mariotto, G., 2024. Deep-UV Raman spectroscopy: a novel heuristic method to characterize volcanologically relevant glasses on Mars. Chem. Geol. 644, 121867.

Cole, D.R., Ross, N.L., 2021. Exploring Earth and planetary materials with neutrons. Elements 17 (3). ISSN 1811-5209.

Di Genova, D., Morgavi, D., Hess, K.U., Neuville, D.R., Borovkov, N., Perugini, D., Dingwell, D.B., 2015. Approximate chemical analysis of volcanic glasses using Raman spectroscopy. J. Raman Spectrosc. 46 (12), 1235–1244.

Di Genova, D., Kolzenburg, S., Wiesmaier, S., Dallanave, E., Neuville, D.R., Hess, K.U., Dingwell, D.B., 2017. A compositional tipping point governing the mobilization and eruption style of rhyolitic magma. Nature 552 (7684), 235–238.

Di Genova, D., Caracciolo, A., Kolzenburg, S., 2018. Measuring the degree of "nanotilization" of volcanic glasses: Understanding syn-eruptive processes recorded in melt inclusions. Lithos 318-319, 209–218.

Dingwell, D.B., Webb, S.L., 1989. Structural relaxation in silicate melts and non-Newtonian melt rheology in geologic processes. Phys. Chem. Miner. 16 (5), 508–516.

Drewitt, J.W.E., Hennet, L., Neuville, D.R., 2022. From short to medium range order in glasses and melts by diffraction and Raman spectroscopy. Rev. Mineral. Geochem. 87, 55–103.

Dufresne, C.D.M., King, P.L., Dyar, M.D., Dalby, K.N., 2009. Effect of SiO2, total FeO, Fe3+/Fe2+, and alkali elements in basaltic glasses on mid-infrared spectra. Am. Mineral. 94 (11−12), 1580–1590.

Dupree, R., Holland, D., McMillan, P.W., Pettifer, R.F., 1984. The structure of soda-silica glasses: a mas NMR study. J. Non-Cryst. Solids 68 (2–3), 399–410.

Farges, F., Lefr`ere, Y., Rossano, S., Berthereau, A., Calas, G., Brown, G.E., 2004. The effect of redox state on the local structural environment of iron in silicate glasses: a combined XAFS spectroscopy, molecular dynamics, and bond valence study. J. Non-Cryst. Solids 344, 176–188.

Ferraro, J.R., Nakamoto, K., Brown, C.W., 2003. Introductory Raman Spectroscopy, Second edition. Elsevier Science, p. 483.

Giordano, D., González-García, D., Russell, J.K., et al., 2020. A calibrated database of Raman spectra for natural silicate glasses: implications for modelling melt physical properties. J. Raman Spectrosc. 51, 1822–1838.

González-García, D., Giordano, D., Russell, J.K., Dingwell, D.B., 2020. A Raman spectroscopic tool to estimate chemical composition of natural volcanic glasses. Chem. Geol. 556 (April), 119819.

Gunde, M.K., 2000. Vibrational modes in amorphous silicon dioxide. Phys. B Condens. Matter 292 (3–4), 286–295.

Henderson, G.S., Calas, G., Stebbins, J.F., 2006. The structure of silicate glasses and melts. Elements 2, 269–273.

Herzberg, G., 1984. Infrared and Raman Spectra of Polyatomic Molecules. D. Van Nostrand, New York xii + 632 pp.

Kalampounias, A.G., Nasikas, N.K., Papatheodorou, G.N., 2009. Glass formation and structure in the MgSiO3–Mg2SiO4 pseudobinary system: from degraded networks to ioniclike glasses. J. Chem. Phys. 131 (11), 114513.

Kilymis, D., Ispas, S., Hehlen, B., Peuget, S., Delaye, J.-M., 2019. Vibrational properties of sodosilicate glasses from first-principles calculations. Phys. Rev. B Condens. Matter 99, 054290.

King, P.L., McMillan, P.F., Moore, G.M., Ramsey, M., Swayze, G., 2004. Infrared spectroscopy of silicate glasses with application to natural systems. Infrared Spectrosc. Geochem. Explor. Geochem. Rem. Sens. 33, 93–133.

Le Losq, C., Neuville, D.R., 2013. Effect of the Na/K mixing on the structure and the rheology of tectosilicate silica-rich melts. Chem. Geol. 346, 57–71.

Le Losq, C., Neuville, D.R., 2017. Molecular structure, configurational entropy and viscosity of silicate melts: link through the Adam and Gibbs theory of viscous flow. J. Non-Cryst. Solids 463, 175–188.

Le Losq, C., Sossi, P.A., 2023. Atomic structure and physical properties of peridotite glasses at 1 bar. Front. Earth Sci. 11.

Le Losq, C., Valentine, A.P., Mysen, B.O., Neuville, D.R., 2021. Structure and properties of alkali aluminosilicate glasses and melts: insights from deep learning. Geochim. Cosmochim. Acta 314, 27–54.

Lemaitre, R.W., Streckeisen, A., Zanettin, B., LeBas, M.J., Bonin, B., Bateman, P., Bellinei, G., Dudek, A., Efremova, S., Keller, J., Lameyre, J., Sabine, P.A., Schmid, R., Sorensen, H., Wooley, A., 2002. Igneous Rocks: A Classification and Glossary of Terms. Recommendations of the International Union of Geological Sciences, Cambridge University Press, NY (USA).

Long, D.A., 1977. Raman Spectroscopy. McGraw-Hill, New York.

Maekawa, H., Maekawa, T., Kawamura, K., Yokokawa, T., 1991. The structural groups of alkali silicate glasses determined from 29Si MAS-NMR. J. Non-Cryst. Solids 127 (1), 53–64.

McMillan, P., 1984. Structural studies of silicate glasses and melts-applications and limitations of Raman spectroscopy. Am. Mineral. 69 (7–8), 622–644.

Meneses, D.D.S., Eckes, M., del Campo, L., Santos, C.N., Vaills, Y., Echegut, P., 2013. Investigation of medium range order in silicate glasses by infrared spectroscopy. Vib. Spectrosc. 65, 50–57.

Mercier, M., Di Muro, A., Giordano, D., Métrich, N., Lesne, P., Pichavant, M., Scaillet, B., Clocchiatti, R., Montagnac, G., 2009. Influence of glass polymerisation and oxidation on micro-Raman water analysis in alumino-silicate glasses. Geochim. Cosmochim. Acta 73 (1), 197–217.

Mercier, M., Di Muro, A., Métrich, N., Giordano, D., Belhadj, O., Mandeville, C.W., 2010. Spectroscopic analysis (FTIR, Raman) of water in mafic and intermediate glasses and glass inclusions. Geochim. Cosmochim. Acta 74 (19), 5641–5656.

Middlemost, E.A.K., 1972. A simple classification of volcanic rocks. Bull. Volcanol. 36, 382–397.

Miletich, R., Malcherek, T., 2005. Mineral structures, defects and their evolution with pressure and temperature in Mineral Behaviour at Extreme Conditions Miletich, R, eds. EMU Notes Mineral. 7, 31–64.

Minitti, M.E., Hamilton, V.E., 2010. A search for basaltic-to-intermediate glasses on mars: Assessing Martian crustal mineralogy. Icarus 210 (1), 135–149.

Mocioiu, O.C., Popa, M., Neacsu, E.I., Zaharescu, M., 2013. Correlation of structural units and chemical stability in SiO₂–PbO–Na₂O ternary glasses: spectroscopic methods. J. Non-Cryst. Solids 361, 130–141.

Morlok, A., Klemme, S., Weber, I., Stojic, A., Sohn, M., Hiesinger, H., 2017. IR spectroscopy of synthetic glasses with Mercury surface composition: Analogs for remote sensing. Icarus 296, 123–138.

Moulton, B.J.A., Henderson, G.S., 2021. Glasses: Alkali and Alkaline-Earth Silicates. In: Encyclopedia of Materials: Technical Ceramics and Glasses, 2, pp. 462–482.

Mysen, B.O., 1983. The structure of silicate melts. Annu. Rev. Earth Planet. Sci. 11, 75–97.

Mysen, B.O., 1990. Role of Al in depolymerized, peralkaline aluminosilicate melts in the systems Li₂O-Al₂O₃-SiO₂, Na₂O-Al₂O₃-SiO₂, and K₂O-Al₂O₃-SiO₂. Am. Mineral. 75 (1–2), 120–134.

Mysen, B., Richet, P., 2005. Silicate Glasses and Melts. Elsevier, Amsterdam, p. 560.

Mysen, B.O., Finger, L.W., Virgo, D., Seifert, F.A., 1982. Curve-fitting of Raman spectra of silicate glasses. Am. Mineral. 67 (7–8), 686–695.

Neuville, D.R., 2006. Viscosity, structure and mixing in (Ca, Na) silicate melts. Chem. Geol. 229 (1–3), 28–41.

Neuville, D.R., Cormier, L., Massiot, D., 2004. Al environment in tectosilicate and peraluminous glasses: a 27Al MQ-MAS NMR, Raman, and XANES investigation. Geochim. Cosmochim. Acta 68 (24), 5071–5079.

Neuville, D.R., Cormier, L., Massiot, D., 2006. Al coordination and speciation in calcium aluminosilicate glasses: Effects of composition determined by 27Al MQ-MAS NMR and Raman spectroscopy. Chem. Geol. 229 (1–3), 173–185.

Neuville, D.R., de Ligny, D., Henderson, G.S., 2014. Advances in Raman spectroscopy applied to Earth and material sciences. Rev. Mineral. Geochem. 78 (1), 509–541.

Neuville, D.R., Henderson, G.S., Dingwell, D.B., 2022. Geological melts. Rev. Mineral. Geochem. 87, 1–1088.

Onodera, Y., Takimoto, Y., Hijiya, H., Taniguchi, T., Urata, S., Inaba, S., Fujita, S., Obayashi, I., Hiraoka, Y., Kohara, S., 2019. Origin of the mixed alkali effect in silicate glass. NPG Asia Mater. 11 (1).

Pisello, A., Vetere, F.P., Bisolfati, M., Maturilli, A., Morgavi, D., Pauselli, C., Iezzi, G., Lustrino, M., Perugini, D., 2019. Retrieving magma composition from TIR spectra: implications for terrestrial planets investigations. Sci. Rep. 9 (1), 1–13.

Pisello, A., Ferrari, M., De Angelis, S., Vetere, F.P., Porreca, M., Stefani, S., Perugini, D., 2022. Reflectance of silicate glasses in the mid-infrared region (MIR): implications for planetary research. Icarus 388 (March), 115222.

Rho, J., Boogert, A., Smith, M.W.L., Lagage, P.O., Dowell, D., Clark, C.J.R., Peeters, E., Cami, J., 2018. A dust twin of Cas A: cool dust and 21μm silicate dust feature in the supernova remnant G54.1+0.3. Mon. Not. R. Astron. Soc. 479 (4), 5101–5123.

Rull, F., Maurice, S., Hutchinson, I., Moral, A., Perez, C., Diaz, C., Colombo, M., Belenguer, T., Lopez-Reyes, G., Sansano, A., Forni, O., Parot, Y., Striebig, N., Woodward, S., Howe, C., Tarcea, N., Rodriguez, P., Seoane, L., Santiago, A., Vago, J. L., 2017. The Raman laser spectrometer for the ExoMars Rover mission to mars. Astrobiology 17 (6–7), 627–654.

Schröder, S., Rammelkamp, K., Hanke, F., Weber, I., Vogt, D.S., Frohmann, S., Kubitza, S., Böttger, U., Hübers, H.W., 2020. Effects of pulsed laser and plasma interaction on Fe, Ni, Ti, and their oxides for LIBS Raman analysis in extraterrestrial environments. J. Raman Spectrosc. 51 (9), 1667–1681.

Sehlke, A., Whittington, A.G., 2015. Rheology of lava flows on Mercury: an analog experimental study. J. Geophys. Res. Planets 120, 1924–1955.

Spiekermann, G., Steele-MacInnis, M., Kowalski, P.M., Schmidt, C., Jahn, S., 2013. Vibrational properties of silica species in MgO-SiO2 glasses obtained from ab initio molecular dynamics. Chem. Geol. 346, 22–33.

Stabile, P., Sicola, S., Giuli, G., Paris, E., Carroll, M.R.R., Deubener, J., Di Genova, D., 2021. The effect of iron and alkali on the nanocrystal-free viscosity of volcanic melts: a combined Raman spectroscopy and DSC study. Chem. Geol. 559, 119991.

Vetere, F., Iezzi, G., Behrens, H., Cavallo, A., Misiti, V., Dietrich, M., Knipping, J., Ventura, G., Mollo, S., 2013. Intrinsic solidification behaviour of basaltic to rhyolitic melts: a cooling rate experimental study. Chem. Geol. 354, 233–242.

Vetere, F., Iezzi, G., Behrens, H., Holtz, F., Ventura, G., Misiti, V., Cavallo, A., Mollo, S., Dietrich, M., 2015. Glass forming ability and crystallisation behaviour of sub-alkaline silicate melts. Earth Sci. Rev. 150, 25–44.

Vetere, F., Rossi, S., Namur, O., Perugini, D., Morgavi, D., Misiti, V., Mancinelli, P., Petrelli, M., Pauselli, C., 2017. Experimental constraints on the rheology, eruption and emplacement dynamics of lavas from Mercury Northern Volcanic Plains. J. Geophys. Res. Planets 122, 1–17.

Vetere, F., Murri, M., Alvaro, M., Domeneghetti, M.C., Rossi, S., Pisello, A., Holtz, F., Perugini, D., 2019. Viscosity of Pyroxenite Melt and its evolution during Cooling: an experimental approach. J. Geophys. Res. Planets 124.

Welsch, A.M., Knipping, J.L., Behrens, H., 2017. Fe-oxidation state in alkali-trisilicate glasses - a Raman spectroscopic study. J. Non-Cryst. Solids 471 (April), 28–38.